Supporting Information

A General Approach for Hierarchically Porous Metal/N/C Nanospheres Electrocatalysts: Nano-Confined Pyrolysis of In-Situ Formed Amorphous Metal-Ligand Complex

*Luming Wu,[a] Baoxia Ni,[a] Rui Chen,[a] Pingchuan Sun,[b] Tiehong Chen [a,]**

[a] Institute of New Catalytic Materials Science, School of Materials Science and Engineering, Key Laboratory of Advanced Energy Materials Chemistry (MOE), Nankai University, Tianjin 300350, PR China.

[b] Key Laboratory of Functional Polymer Materials of Ministry of Education, College of Chemistry, Nankai University, Tianjin 300071, PR China.

E-mail: chenth@nankai.edu.cn.

1. Experimental Section

1.1 Chemicals and materials

All the reagents were of analytical grade and used as received without further purification. Zinc chloride ($ZnCl_2$), Zinc oxide (ZnO), 2-methylimidazole (2-MeIM), ferrous oxalate ($FeC_2O_4{\cdot}2H_2O$), 1, 10-Phenanthroline monohydrochloride monohydrate (Phen), tetraethyl orthosilicate (TEOS), and hydrofluoric acid (HF, 40%) were obtained from Sigma-Aldrich (Shanghai, China). Poly (acrylic acid) (PAA) (average molecular weight 240,000, 25 wt %) was purchased from Alfa Aesar. Cetyltrimethylammonium bromide (CTAB) and ammonia (25 wt% aqueous solution) were purchased from Macklin. The commercial Pt/C catalyst (loading of 20 wt%) was supplied by Alfa Aesar. Nafion (5% in a mixture of lower aliphatic alcohols and water) was acquired from Sigma-Aldrich.

1.2 Preparation

Hierarchically mesoporous silica spheres (NKM-5) were prepared according to our previously reported method. [1] The Fe/N/C-HP was synthesized by the following pyrolysis process. Typically, appropriate amount of NKM-5, 2-MeIM, $ZnCl_2$, $FeC_2O_4{\cdot}2H_2O$ and Phen (the mole ratio of MeIM and znic ions was fixed at 3.0, the mole ratios of Phen and $FeC_2O_4{\cdot}2H_2O$ was fixed to 3.0, and the mole ratios of znic ions and $FeC_2O_4{\cdot}2H_2O$ was fixed to 30.0) were placed in glove box full of argon. The resulting dry powder were uniformly mixed by ball-milled for 2×30 min at 400 rpm under argon

protection. The obtained solid mixture was placed in a quartz boat in a tube furnace and thermally treated at 950 °C for 3 hours under nitrogen atmosphere at a ramping rate of 5 °C min^{-1}. The pyrolyzed products were etched in HF solution (10 wt%) to simultaneously remove the silica templates and inactive Fe-containing species. The obtained sample was denoted as Fe/N/C-HP. To determine the optimum conditions for the formation of Fe/N/C-HP catalysts, different pyrolysis temperatures (750, 850 and 1050 °C) were examined. The obtained samples were denoted as Fe/N/C-HP_{750}, Fe/N/C-HP_{850} and Fe/N/C-HP_{1050}, respectively. Different iron and zinc molar ratios are prepared to obtain the optimal iron doping amount (molar ratios of Fe:Zn=1:20, 1:30, 1:40 and 1:50 represent are recorded as Fe/N/C-HP-1/20, Fe/N/C-HP, Fe/N/C-HP-1/40 and Fe/N/C-HP-1/50). The hierarchically porous nitrogen-doped carbon nanospheres (HPNC) was prepared with same process of Fe/N/C-HP but in the absence of $FeC_2O_4 \cdot 2H_2O$ and Phen.

1.3 Characterizations

Field-emission scanning electron microscopy (FESEM; JEOL, JSM-7800F, 15 kV) was used to analyze the surface morphology of catalysts. Transmission electron microscopy (TEM) measurements was performed on a JEM-2800 microscope, working at 200 kV. Samples were ultrasonically dispersed in ethanol solution and dropped onto copper grids to conduct TEM measurements. The Powder X-ray diffraction (XRD) patterns of samples were obtained from a Rigaku Smart Lab 3kW powder diffractometer using Cu Kα radiation. The Raman spectra were obtained by a Raman spectrometer (SR-500I-A) using laser excitation at 532 nm. X-ray photoelectron spectroscopy (XPS, Thermo Scientific ESCALAB 250Xi spectrometer) was applied to measurement surface information of samples. The Brunauer–Emmett–Teller (BET-Autosorb-iQ2) specific surface area of the catalysts was measured from the nitrogen adsorption–desorption isotherms. The pore size distribution plot was recorded from the adsorption branch of the isotherm based on the Density Functional Theory (DFT). The contents of Fe was determined by inductively coupled plasma-atomic emission spectrometry (ICP-AES) on a Thermo Jarrell-Ash ICP-9000. The Fe K-edge X-ray absorption spectra (XAS) including X-ray absorption near-edge (XANES) and extended X-ray adsorption fine structure (EXAFS) were collected at the Singapore Synchromator Light Source (SSLS) center, where a pair of channel-cut Si (111) crystals was used in the monochromator. The Fe K-edge XAS data were recorded in a transmission mode. Fe foil, Fe_3O_4 and FeO were used as references. The storage ring was working at the energy of 2.5 GeV with an

average electron current of below 200 mA. The acquired EXAFS data were extracted and processed according to the standard procedures using the ATHENA module implemented in the IFEFFIT software packages. The k2-weighted Fourier transform (FT) of x (k) in R space was obtained over the range of 0-14.0 $Å^{-1}$ by applying a Bessel window function.

1.4 Electrochemical measurements

1.4.1 Rotating disk electrode (RDE) measurement

The electrochemical properties were studied by a rotating ring-disk electrode (RRDE-3A, ALS, Japan) in conjunction with a CHI660D electrochemical workstation at room temperature with a three-electrode system. A glassy carbon (GC) rotating disk electrode (RDE) coated with catalysts was used as working electrode, graphite rod and Ag/AgCl (3 M KCl) were used as counter and reference electrode, respectively. Typically, 8 mg of sample was mixed with 800 μL H_2O, 180 μL isopropanol, and 20 μL 5 wt% Nafion solution by sonication for 60 min to form a homogeneous catalyst ink. Then 15 μL of the ink was carefully dropped with pipettor onto a rotation disk electrode (RDE) (5 mm inner diameter) which was polished and washed before use (loading 600 μg cm^{-2}). Then, the RDE was dried in air to allow solvent evaporation at room temperature. Potentials in this work were all calibrated with respect to the reversible hydrogen electrode (RHE) before use. Before the test, N_2 (or O_2) was bubbled into the electrolyte for at least 30 min and the N_2- (or O_2) was kept bubbling during the measurements. For ORR, the LSV curves were recorded at a scan rate of 5 $mV \cdot s^{-1}$. All of the LSV curves were recorded after subtraction of the background current recorded in N_2-saturated solution. The chronoamperometric measurement (i-t) was tested to investigate the electrode stability at the bias potential of -0.5 V (vs. Ag/AgCl) in O_2-saturated 0.1 M KOH or at 0.3 V (vs. Ag/AgCl) in O_2-saturated 0.1 M $HClO_4$ with a rotation rate of 1600 rpm, respectively. The tolerance of a catalyst to methanol crossover was tested by adding 5 mL methanol into the O_2-saturated electrolyte solution. For comparison, the general loading of the benchmark commercial (20 wt % Pt) Pt/C catalyst on the work electrode was 150 μg cm^{-2} in both alkaline and acidic media. RDE polarization curves were collected at disk rotation rates of 900, 1225, 1600, 2025 and 2500 rpm. The electrons transfer number (n) was calculated on the basis of the Koutecky–Levich equation:

$$J^{-1}=J_K^{-1}+J_L^{-1} = (nFkC_0)^{-1} + (0.62nFC_0D_0^{2/3}\upsilon^{-1/6}\omega^{1/2})^{-1}$$

Where J is the measured disk current density, J_K and J_L are the kinetic and diffusion limiting current

densities, the current densities and kinetic current densities reported in the manuscript were obtained by normalizing the geometric area of the electrode. F is the Faraday constant (96500 C mol^{-1}), ω is the angular velocity, n is the number of electrons transfer per oxygen molecular, C_0 is the bulk concentration of O_2 in the electrolyte (1.2×10^{-3} mol L^{-1}), D_0 is the diffusion coefficient of O_2 in the electrolyte (1.9×10^{-5} cm^{-2} s^{-1}), υ is the kinematic viscosity of the electrolyte (1.0×10^{-2} cm^{-2} s^{-1}), and k is the electron-transfer rate constant.

1.4.2 Rotating ring-disk electrode (RRDE) measurement

Rotating ring-disk electrode (RRDE) measurement was used to calculate the electron transfer number (n) as well as the H_2O_2 yield during the ORR according to the following formulas:

$$H_2O_2\% = 200 \times (I_r/N)/(I_d + I_r/N)$$

$$n = 4 \times I_d/(I_d + I_r/N)$$

Where I_d is the disk current, I_r is the absolute value of the ring current, and N = 0.37 is the current collection efficiency of Pt ring.

The electrochemically active surface area (ECSA) of the Fe/N/C-HP and Fe/N/C/NC was measured by the non-faradaic double layer capacitance (C_{dl}). The C_{dl} is a quantitative indicator of the surface area that is accessible to the electrolyte ions. Typically, a series of CV curves were measured at various scan rates of 5, 10, 15, 20, 25 and 30 mV/s between 0.95 V and 1.05 V versus RHE. The anodic and cathodic charging currents (i_a and i_c) were recorded in the potential region where there was no faradaic process in N_2-saturated 0.1 M KOH and 0.1 M $HClO_4$. The slope of the linear fitting line was twice of the C_{dl} value, which is proportional to the ECSA of the resulting catalysts.

$$c_{dl} = \frac{i_a + i_c}{v \times 2}$$

The ECSA was calculated as follows:

$$ECSA = \frac{C_{dl}}{C_s}$$

Where C_s is the general specific capacitance for an atomically smooth planar surface under homogeneous electrolyte conditions. The C_s value is adopted as 0.04 mF cm^{-2} [2] and 0.02 mF cm^{-2} [3] in 0.1 M KOH and 0.1 M $HClO_4$, respectively.

1.4.3 RHE calibration

We used Ag/AgCl (3 M KCl) as the reference electrode in all measurements. It was calibrated

with respect to reversible hydrogen electrode (RHE). The calibration was performed in the high purity hydrogen saturated electrolyte with a Pt wire as the working electrode. CVs were run at a scan rate of 1 mV s^{-1}, and the average of the two potentials at which the current crossed zero was taken to be the thermodynamic potential for the hydrogen electrode reactions.

a) 0.1 M KOH

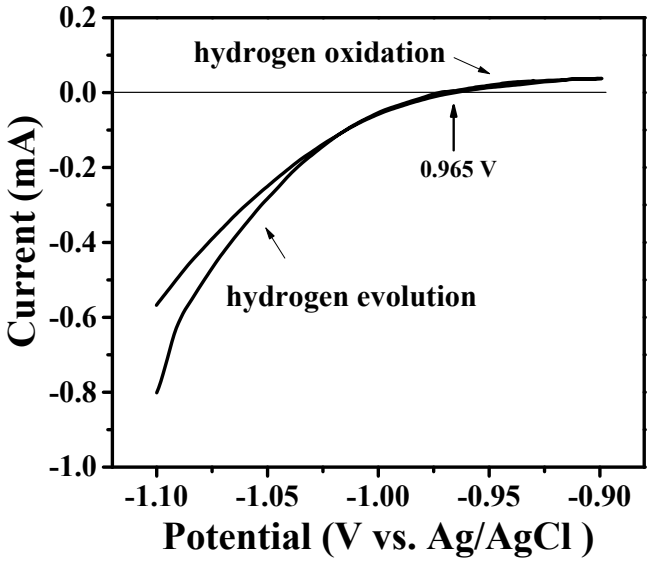

Fig. S1. The potential calibration of Ag/AgCl electrode compared with reversible hydrogen electrode (RHE) in 0.1 M KOH.

So in 0.1 M KOH, E (RHE) = E(Ag/AgCl)+0.965 V

b) 0.1 M $HClO_4$

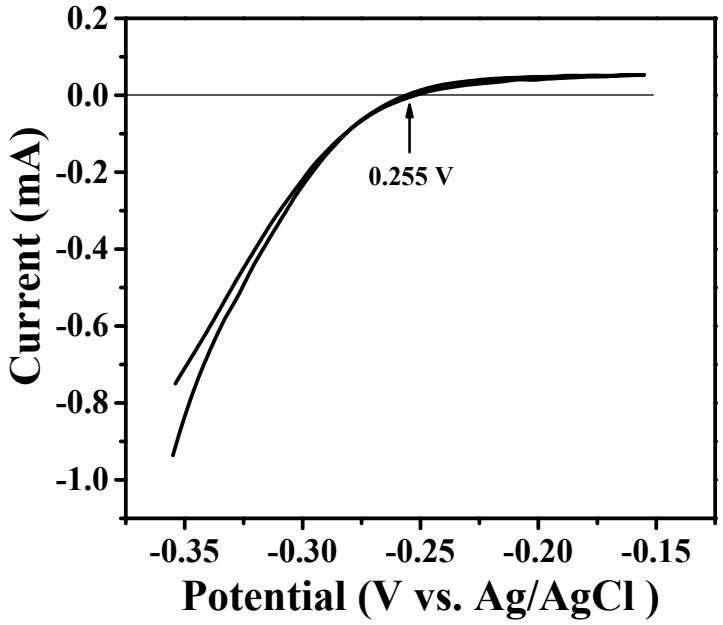

Fig. S2. The potential calibration of Ag/AgCl electrode compared with reversible hydrogen electrode (RHE) in 0.1 M $HClO_4$.

So in 0.1 M $HClO_4$, E (RHE) = E(Ag/AgCl)+0.255 V

1.4.4 A primary Zn-air batteries tests

The primary Zn-air batteries were tested in a home-built electrochemical cell. The homogeneous ink was loaded on carbon paper (1 cm^2), with a loading density of 1 mg cm^{-2}, as the air cathode, and a polished Zn foil was used as the anode. A 0.2 M $Zn(OAc)_2$ in 6 M KOH aqueous solution was used as the electrolyte. The experiment was carried out with a CHI660D electrochemical workstation.

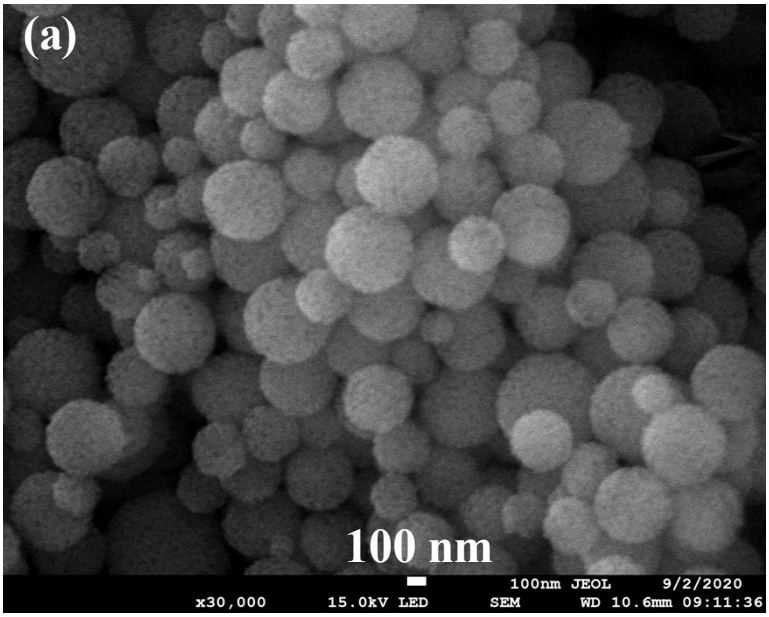

Fig. S3. SEM images of the hierarchically porous silica nanospheres (NKM-5).

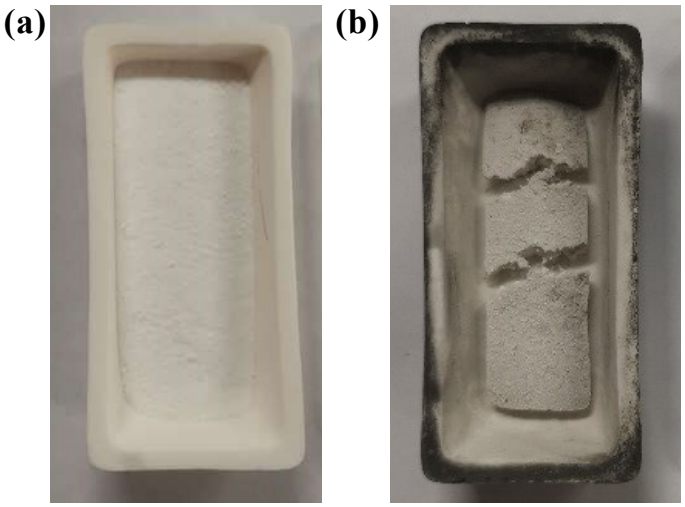

Fig. S4. Photos of (a) mixture of NKM-5 and 2-MeIM before pyrolysis and (b) after pyrolysis.

In photo (b) the product is white because only the silica template was left and no carbon was formed.

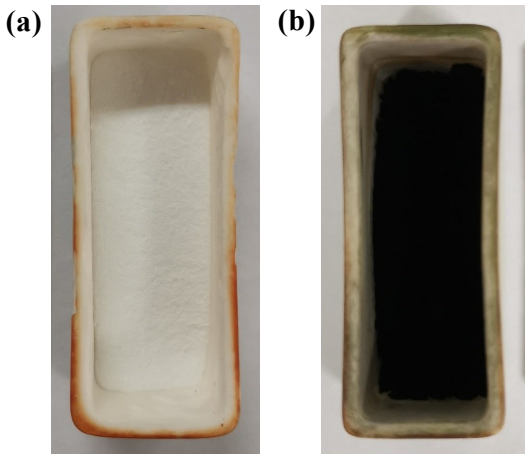

Fig. S5. Photos of synthesis of HPNC. (a) Mixture of NKM-5, $ZnCl_2$, 2-methylimidazole (2-MeIM) before pyrolysis and (b) after pyrolysis.

The product is black because of the carbon formed after pyrolysis.

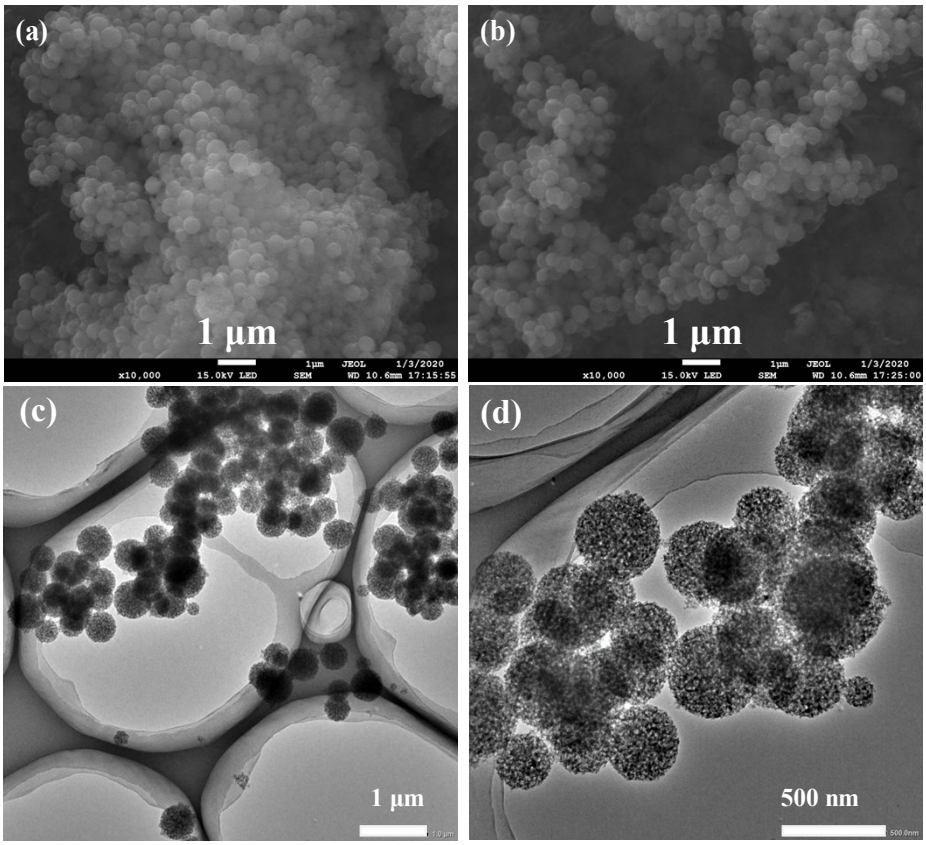

Fig. S6. (a, b) SEM images of HPNC and (c, d) TEM images of HPNC.

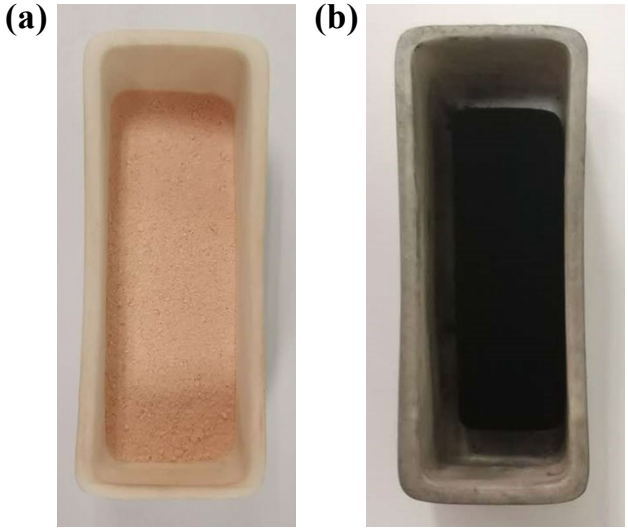

Fig. S7. Photos of synthesis of Fe/N/C-HP. (a) Mixture of NKM-5, $ZnCl_2$, 2-methylimidazole (2-MeIM), ferrous oxalate and 1,10-phenanthroline hydrochloride (Phen) and (b) after pyrolysis. The product is black because of the carbon formed after pyrolysis.

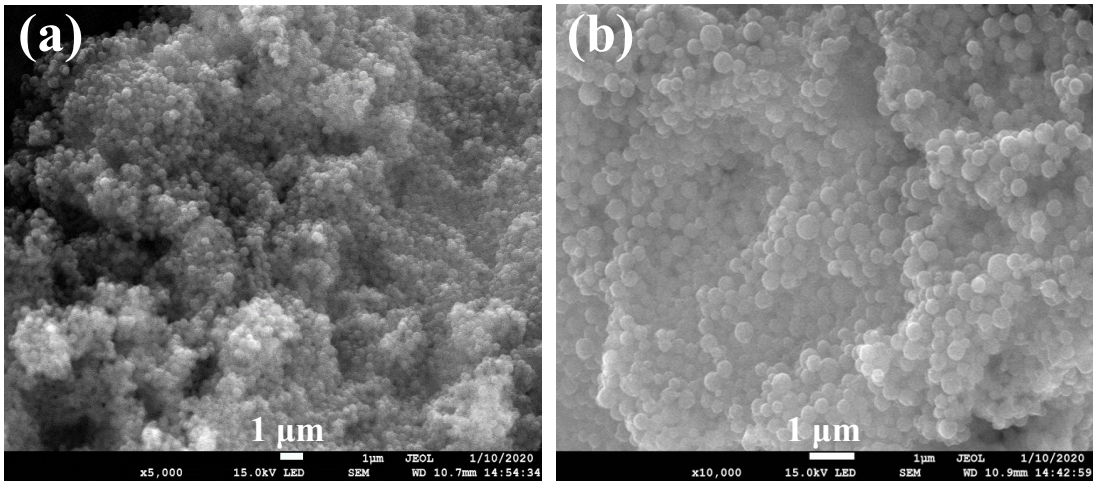

Fig. S8. (a, b) SEM images of Fe/N/C-HP.

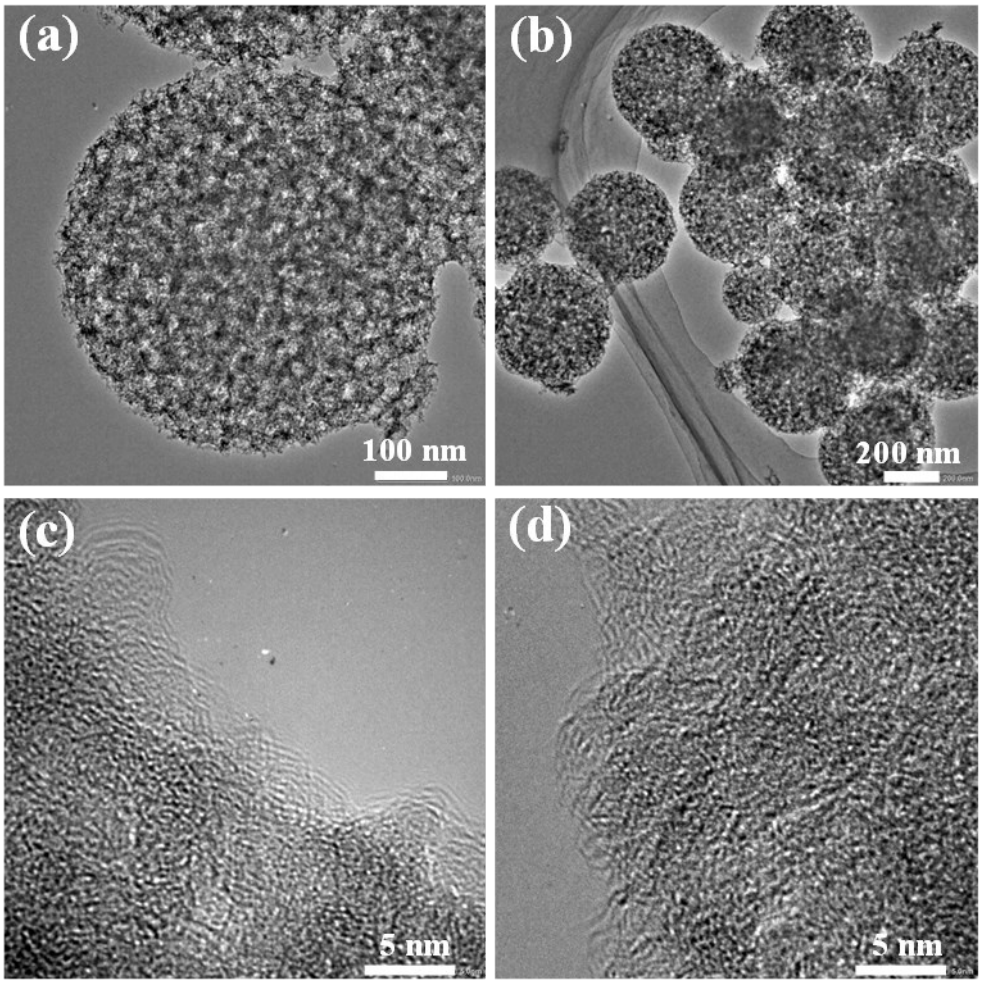

Fig. S9. (a, b) TEM images of Fe/N/C-HP and (c, d) HRTEM images of Fe/N/C-HP.

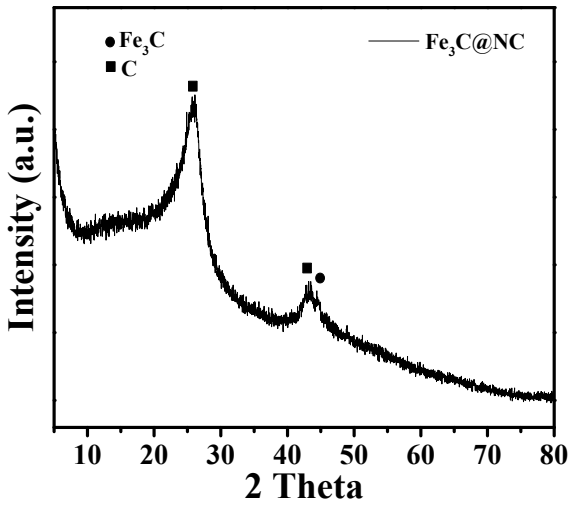

Fig. S10. XRD pattern of Fe_3C@NC.

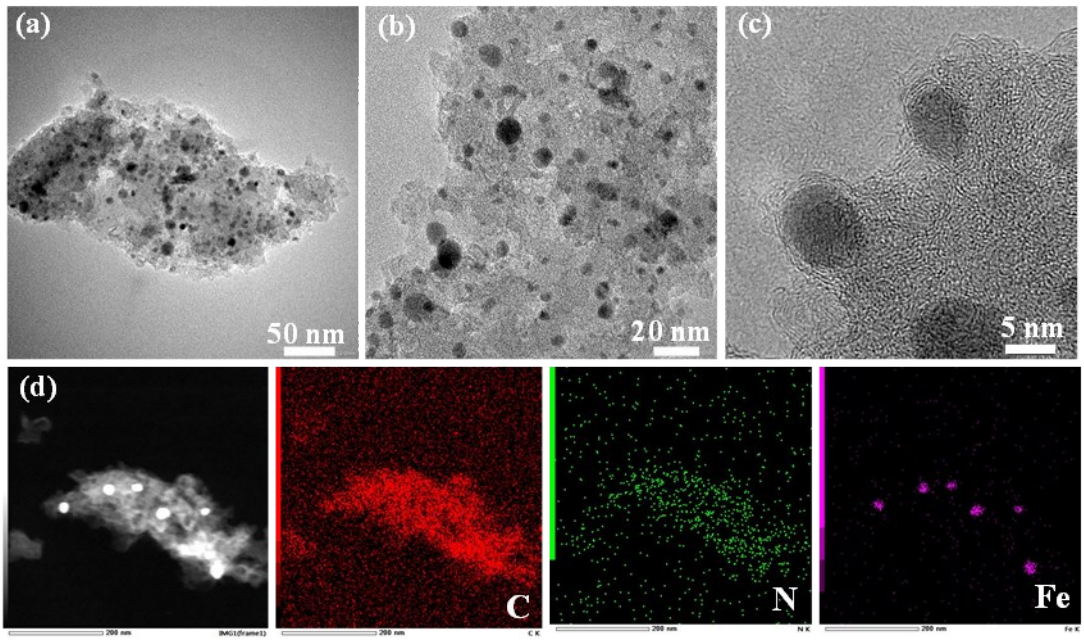

Fig. S11. (a-d) TEM images of Fe_3C@NC and corresponding element mappings.

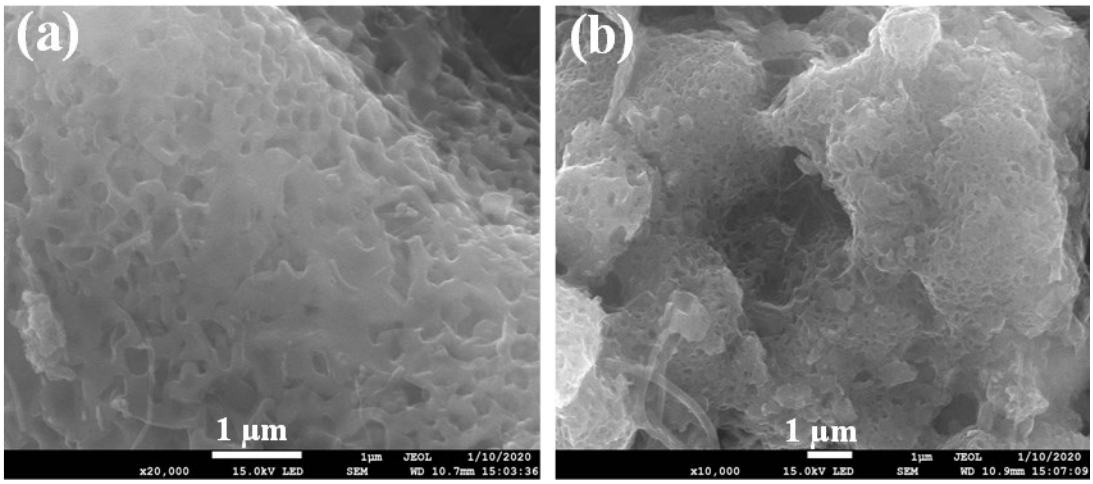

Fig. S12. (a, b) SEM images of Fe/N/C/NC.

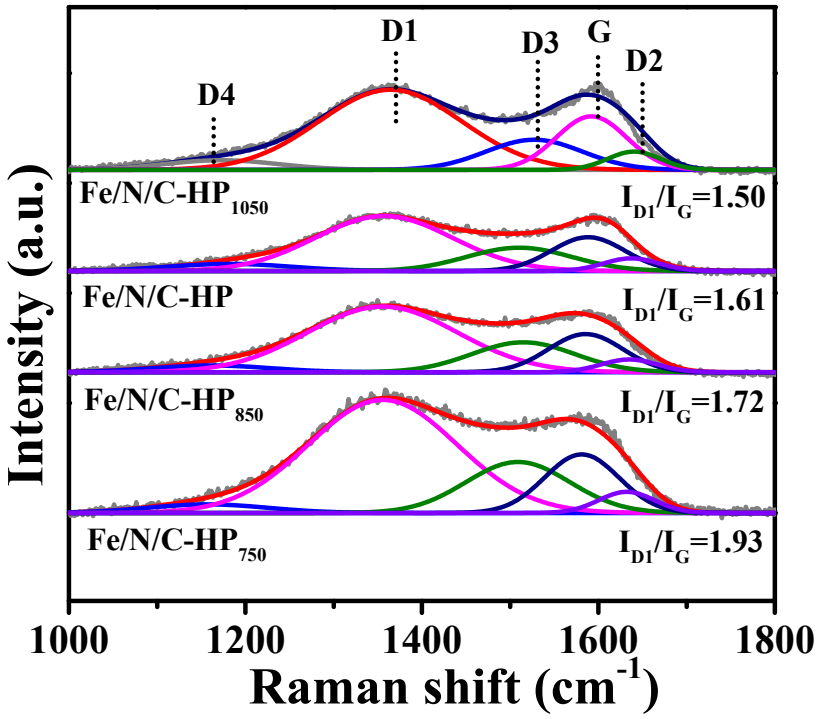

Fig. S13. Raman spectra of Fe/N/C-HP pyrolysis at different temperature.

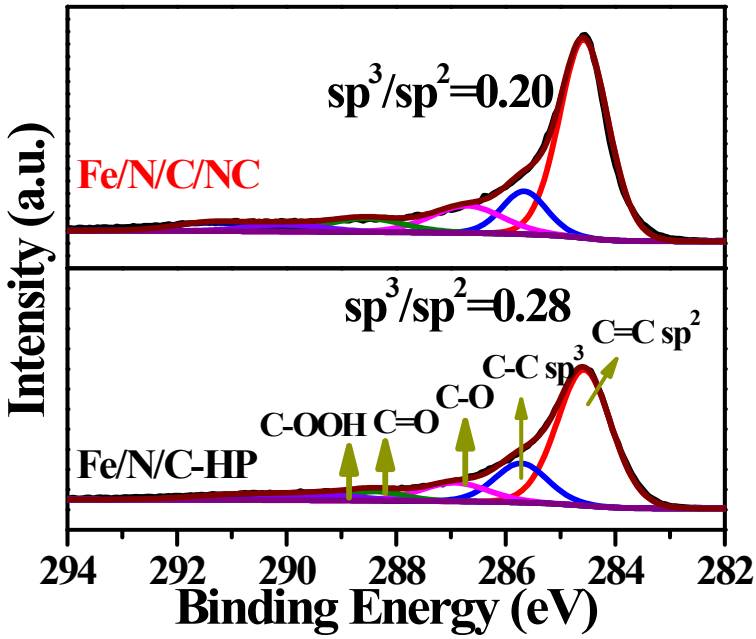

Fig. S14. XPS spectra for the C 1s regions of Fe/N/C-HP and Fe/N/C/NC.

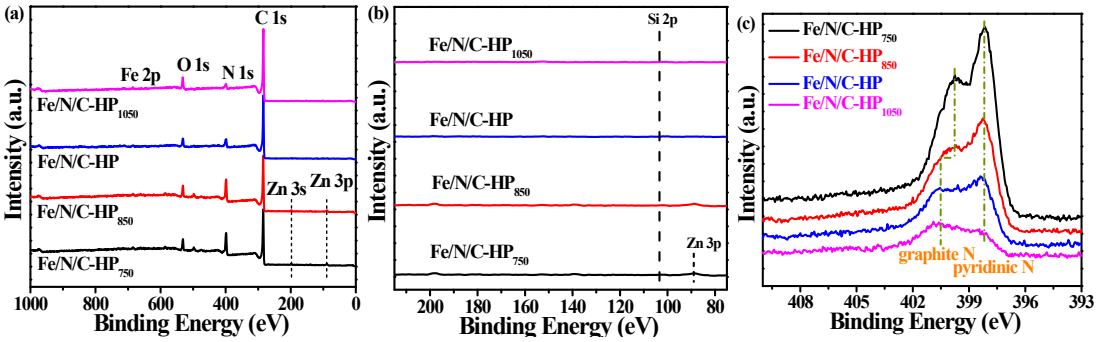

Fig. S15. (a) XPS survey spectra, (b) locally enlarged (×100) and (c) N 1s spectra of Fe/N/C-HP pyrolyzed at different temperatures.

No signal of Si (103.4 eV for Si 2p, the position of the dished line in (b)) in Fe/N/C-HP pyrolysis at different temperature can be observed, indicating that Si element was removed successfully after HF treatment. For the weak peaks at ~89.2 eV and 197.9 eV, they belongs to Zn 3p and Zn 3s, because Zn (vapor temperature: ~907 °C) is not completely volatilized in the samples of Fe/N/C-HP$_{750}$ and Fe/N/C-HP$_{850}$ under pyrolysis temperature of 750 °C and 850 °C.

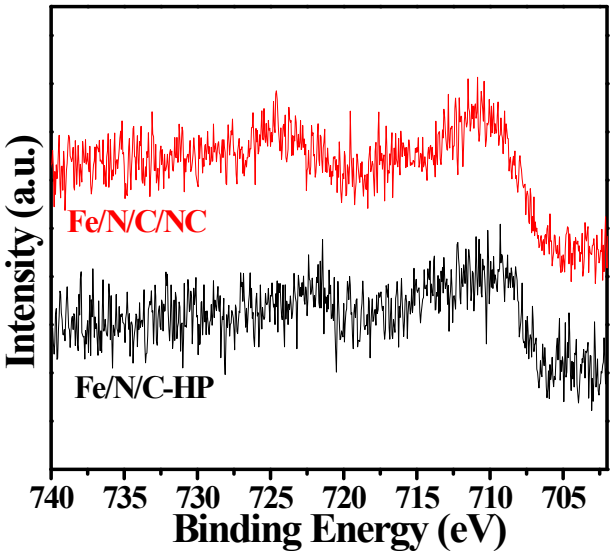

Fig. S16. High-resolution XPS spectra of Fe 2p for Fe/N/C-HP and Fe/N/C/NC.

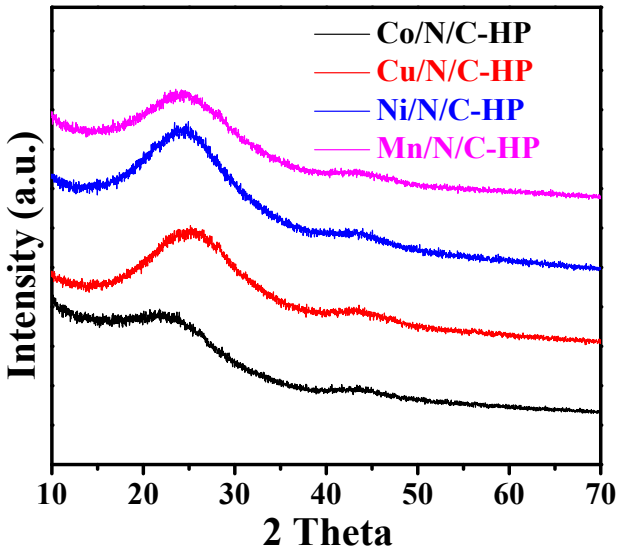

Fig. S17. XRD pattern of Co/N/C-HP, Ni/N/C-HP, Cu/N/C-HP and Mn/N/C-HP.

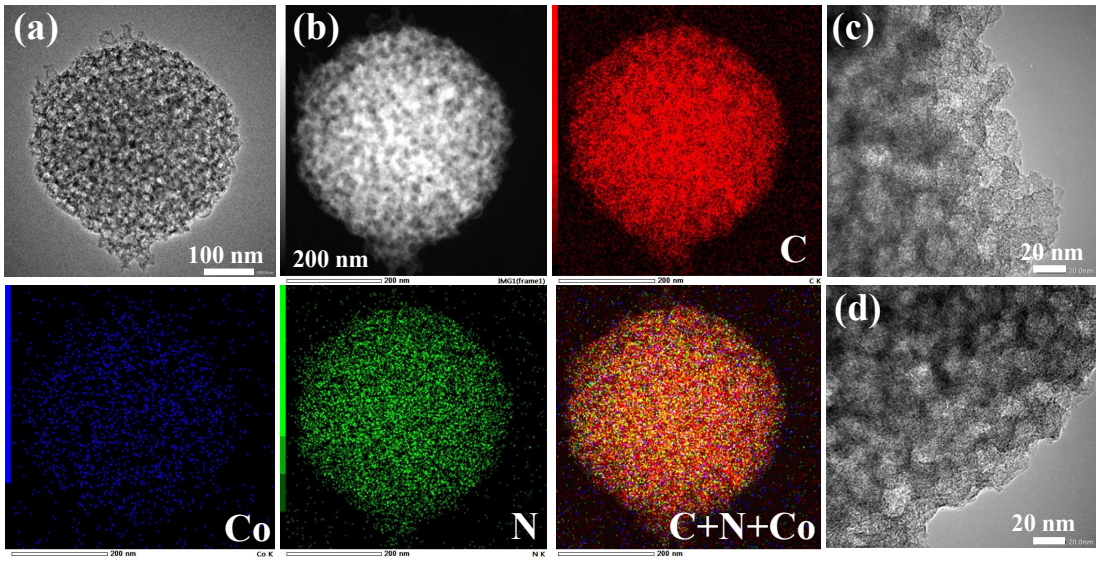

Fig. S18. (a-c) TEM images of Co/N/C-HP and corresponding element mappings.

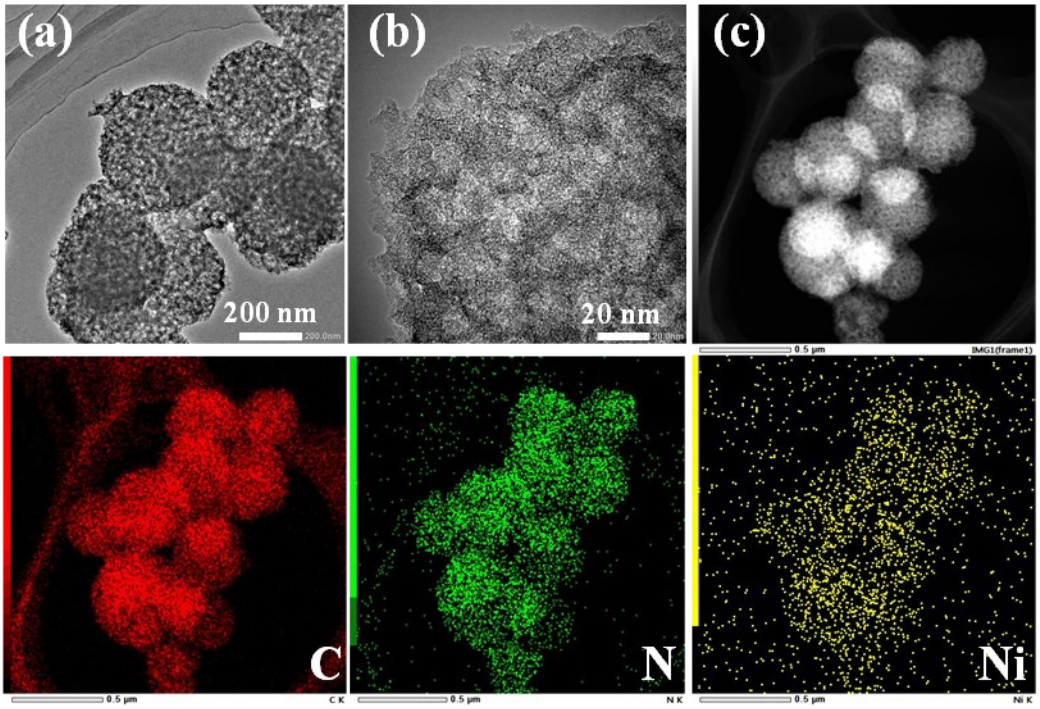

Fig. S19. (a-c) TEM images of Ni/N/C-HP and corresponding element mappings.

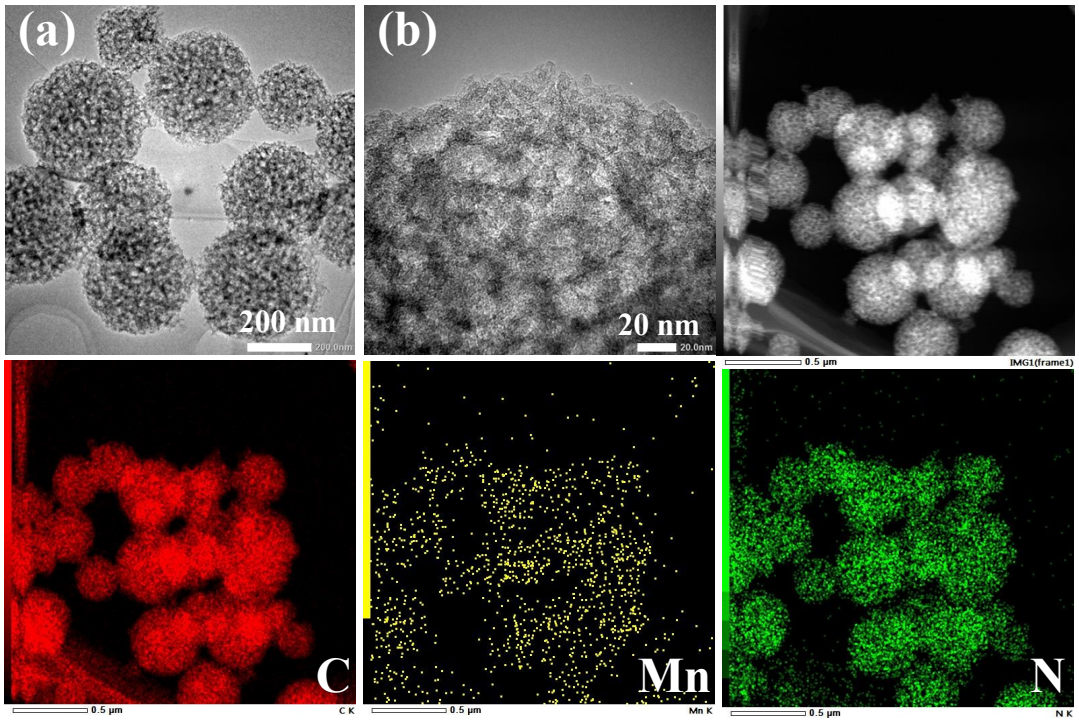

Fig. S20. (a-c) TEM images of Mn/N/C-HP and corresponding element mappings.

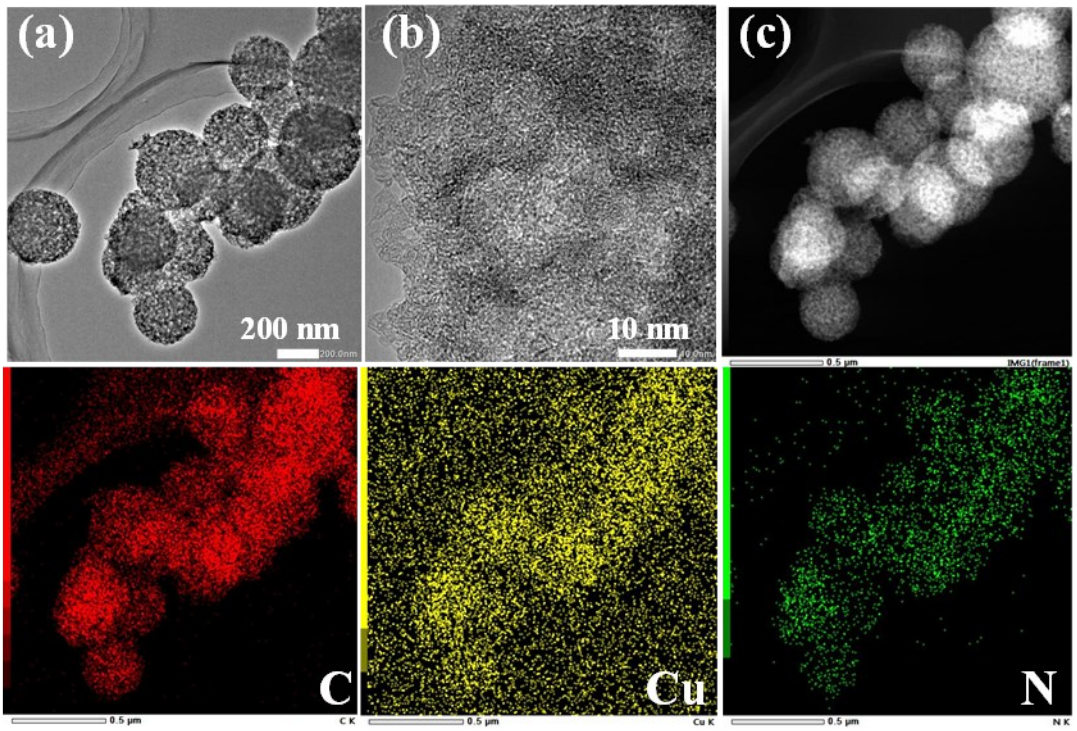

Fig. S21. (a, b) TEM images of Cu/N/C-HP and corresponding element mappings.

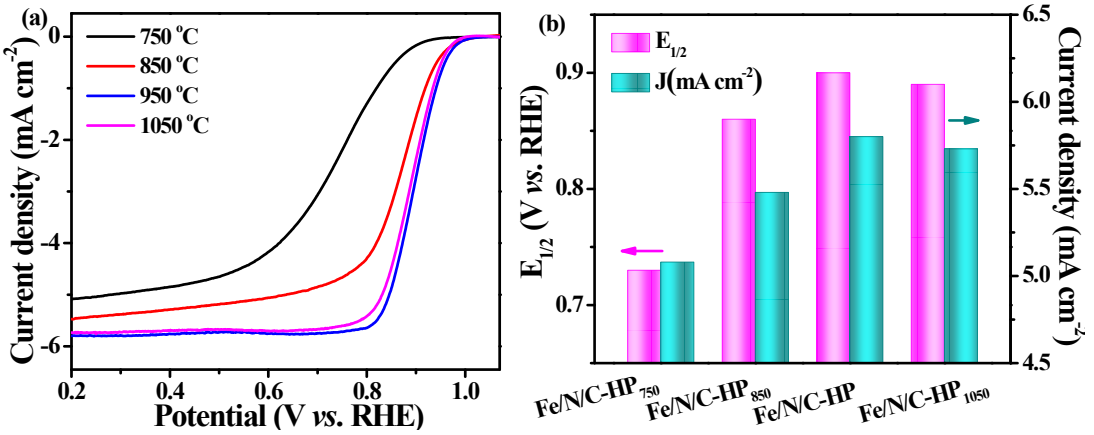

Fig. S22. (a) LSV polarization curves and (b) half-wave potentials and limiting current density of the series Fe/N/C-HP obtained at different annealing temperature in O_2-saturated 0.1 M KOH solution.

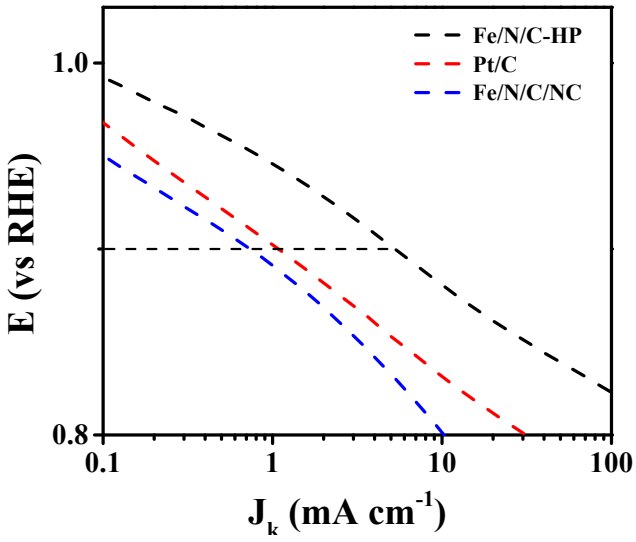

Fig. S23. Electrochemical Tafel curves (E versus log J_k) of Fe/N/C-HP, Pt/C and Fe/N/C/NC in O_2-saturated 0.1 M KOH. RDE experiment at 1600 rpm.

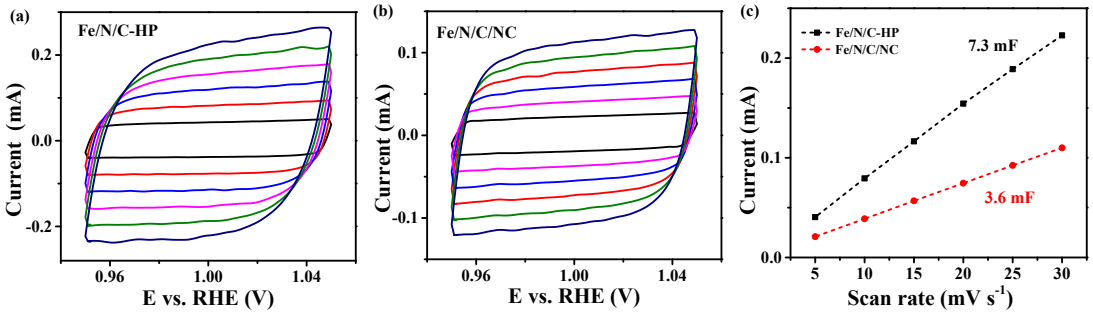

Fig. S24. The electrochemical double layer capacitance (C_{dl}) estimation. Cyclic voltammetry (CV) data of (a) Fe/N/C-HP and (b) Fe/N/C/NC at various scan rates (5-30 mV s^{-1}). (c) Plots of current densities (taken at 1.00 V vs. RHE) as a function of scan rates. All the CV curves were obtained in nitrogen-saturated 0.1 M KOH.

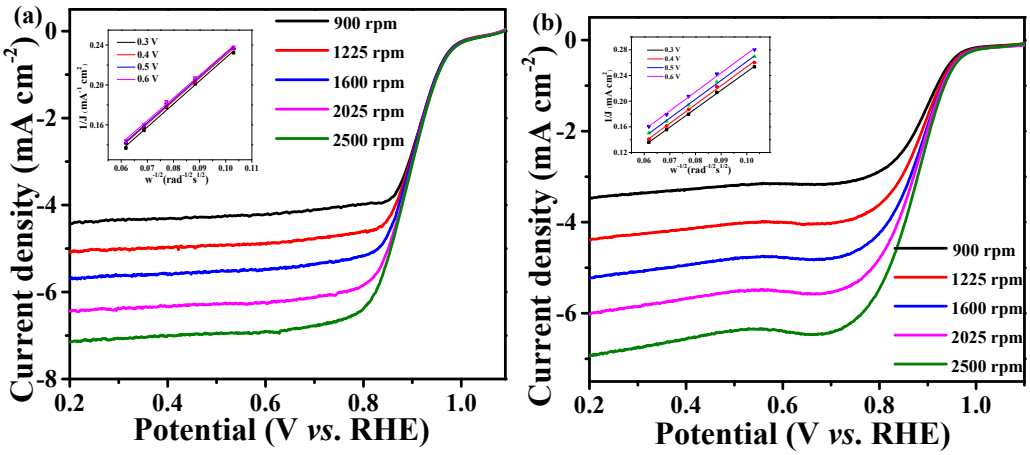

Fig. S25. ORR polarization curves of the developed catalysts under various rotating speeds and their corresponding K-L plots in 0.1 M KOH at 0.3-0.6 V. (a) Fe/N/C-HP and (b) Fe/N/C/NC.

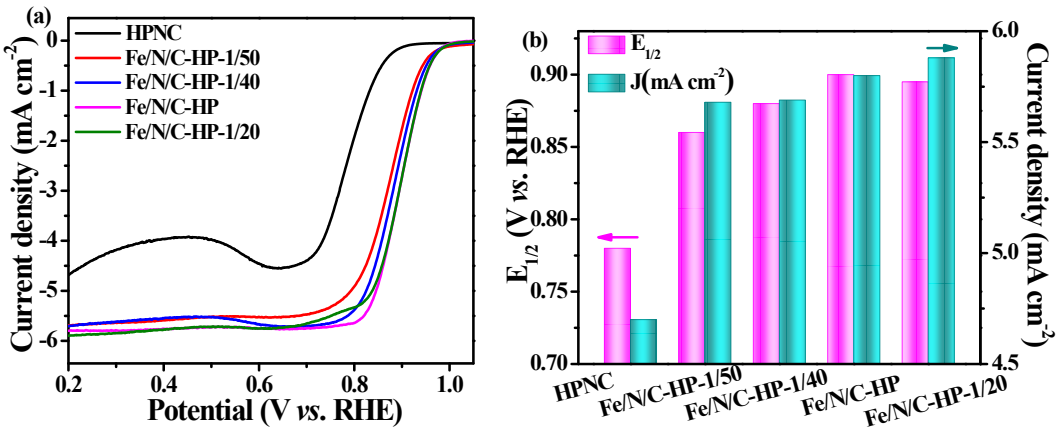

Fig. S26. (a) LSV polarization curves and (b) half-wave potentials and limiting current density of the series Fe/N/C-HP with different Fe contents in 0.1 M KOH.

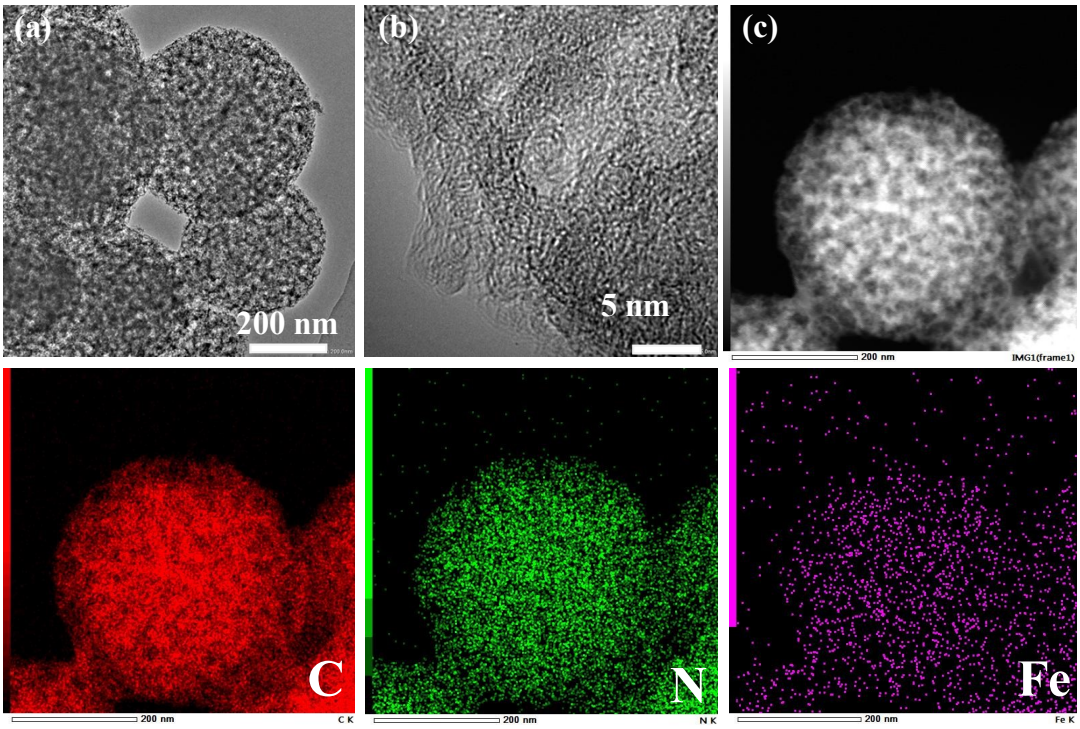

Fig. S27. (a-c) TEM images of pristine Fe/N/C-HP and corresponding element mappings before durability test.

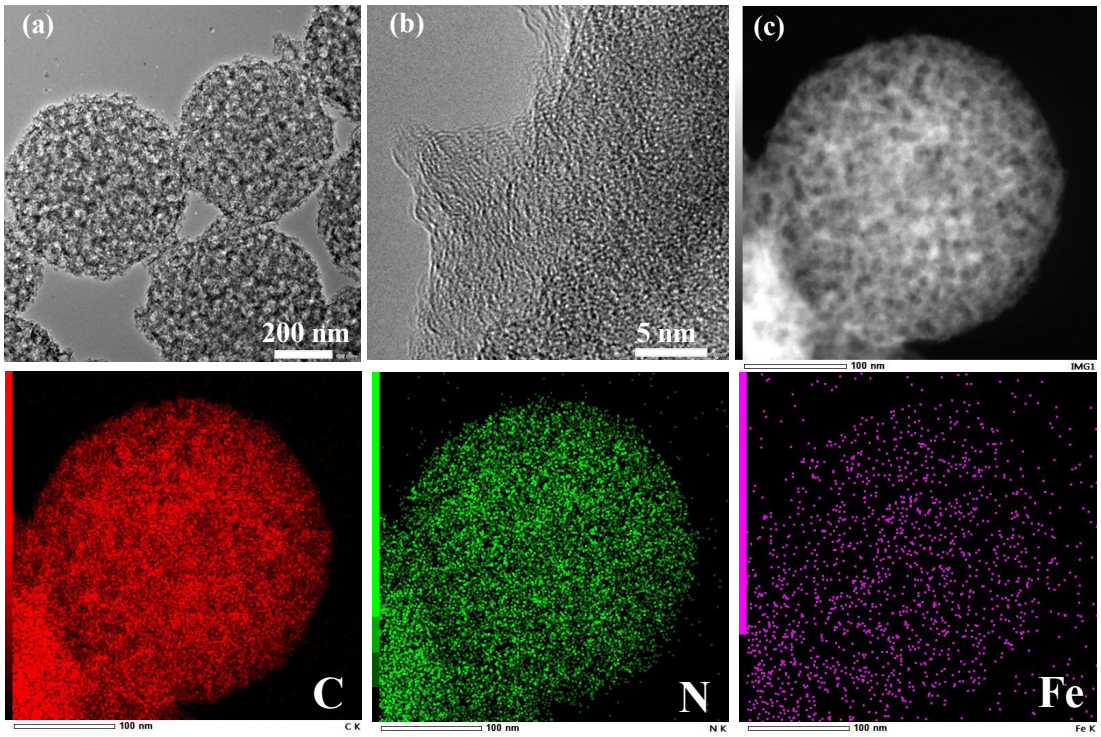

Fig. S28. (a-c) TEM images of Fe/N/C-HP and corresponding element mappings after running 40000 s in 0.1 M KOH.

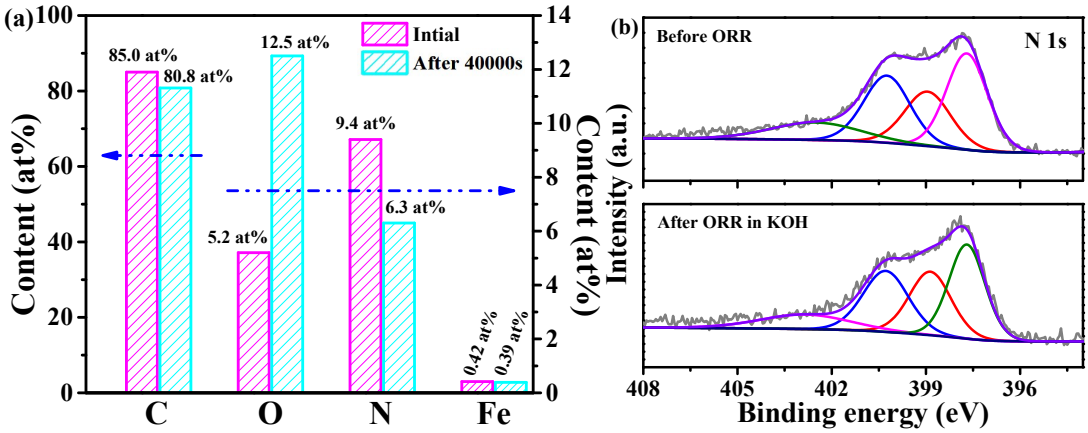

Fig. S29. (a) Elemental composition and (b) N 1s high-resolution XPS spectra of Fe/N/C-HP before and after ORR in 0.1 M KOH.

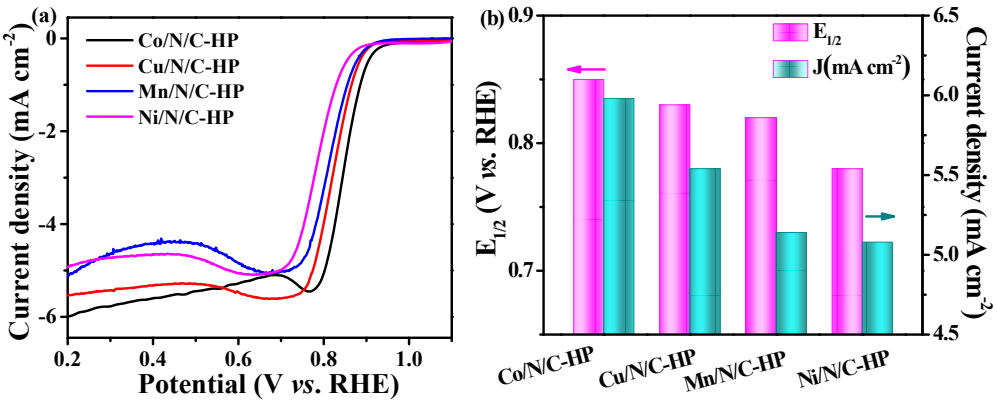

Fig. S30. (a) LSV polarization curves and (b) half-wave potentials and limiting current density of Co/N/C-HP, Mn/N/C-HP, Ni/N/C-HP and Cu/N/C-HP in O_2-saturated 0.1 M KOH.

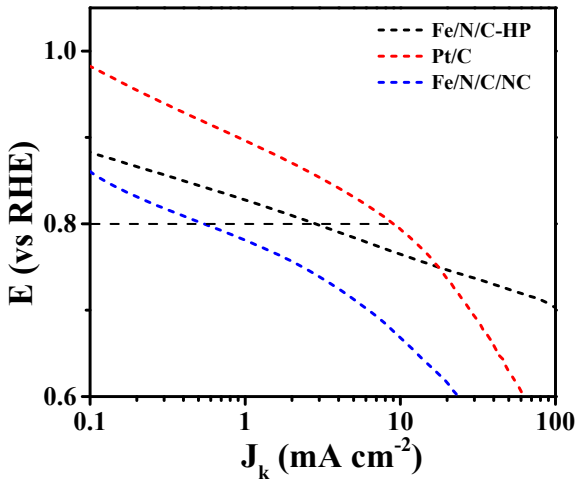

Fig. S31. Electrochemical Tafel curves (applied E versus log J_k) of Fe/N/C-HP, Pt/C and Fe/N/C/NC in O_2-saturated 0.1 M $HClO_4$. RDE experiment at 1600 rpm.

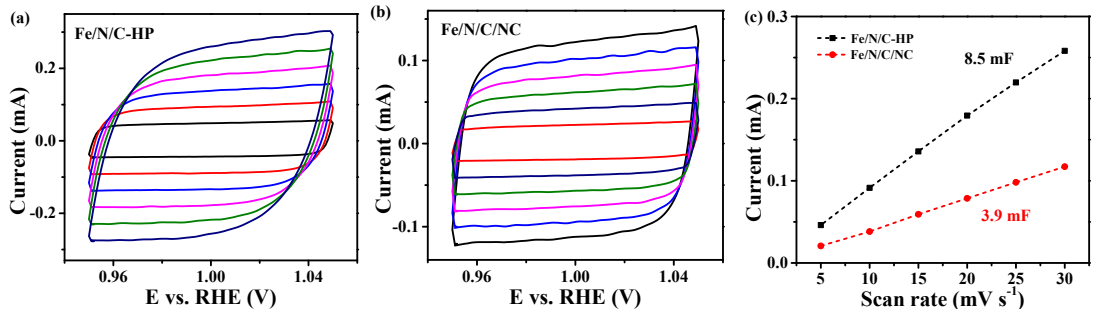

Fig. S32. The electrochemical double layer capacitance (C_{dl}) estimation. Cyclic voltammetry (CV) data of (a) Fe/N/C-HP and (b) Fe/N/C/NC at various scan rates (5-30 mV s^{-1}). (c) Plots of current densities (taken at 1.00 V vs. RHE) as a function of scan rates. All the CV curves were obtained in nitrogen-saturated 0.1 M $HClO_4$.

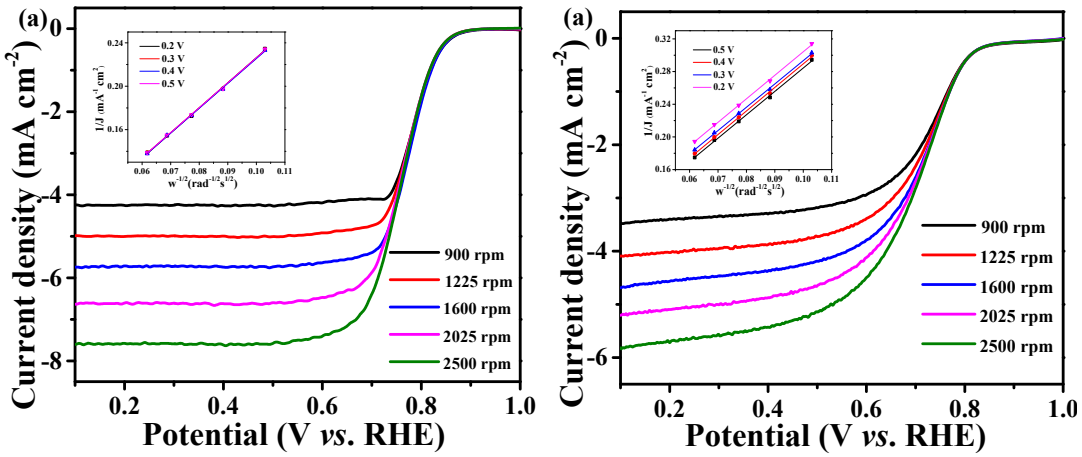

Fig. S33. ORR polarization curves of the developed catalysts under various rotating speeds and their corresponding K-L plots in 0.1 M $HClO_4$ at 0.2-0.5 V. (a) Fe/N/C-HP and (b) Fe/N/C/NC.

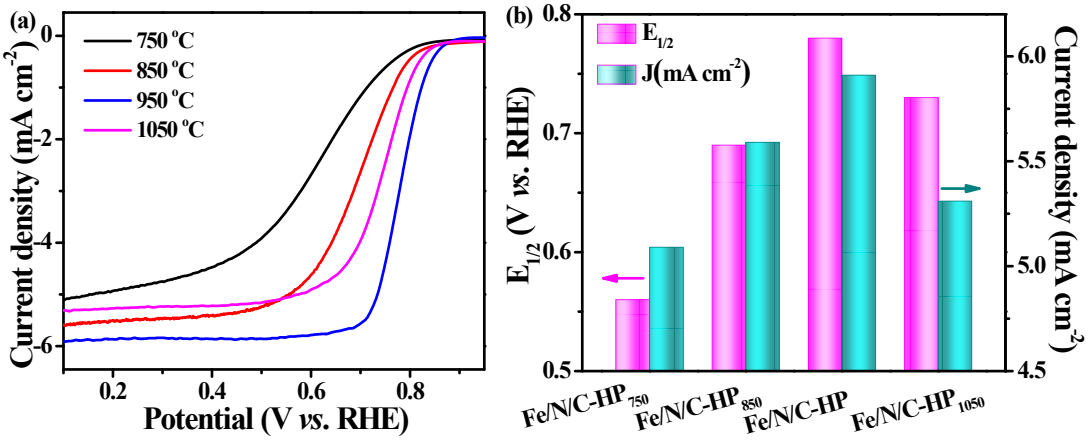

Fig. S34. ORR polarization curves (a) LSV polarization curves and (b) half-wave potentials and limiting current density of Fe/N/C-HP electrocatalysts obtained at different annealing temperature in 0.1 M $HClO_4$.

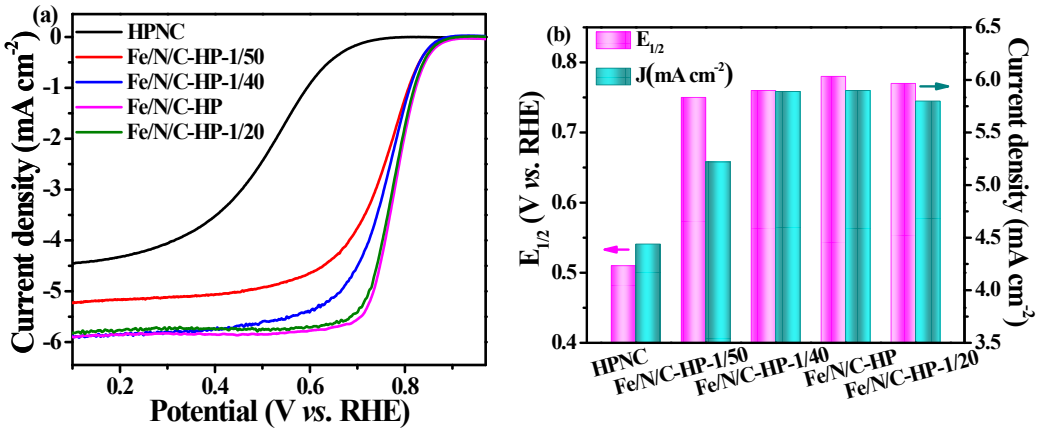

Fig. S35. (a) LSV polarization curves and (b) half-wave potentials and limiting current density of the series Fe/N/C-HP with different Fe contents in 0.1 M $HClO_4$.

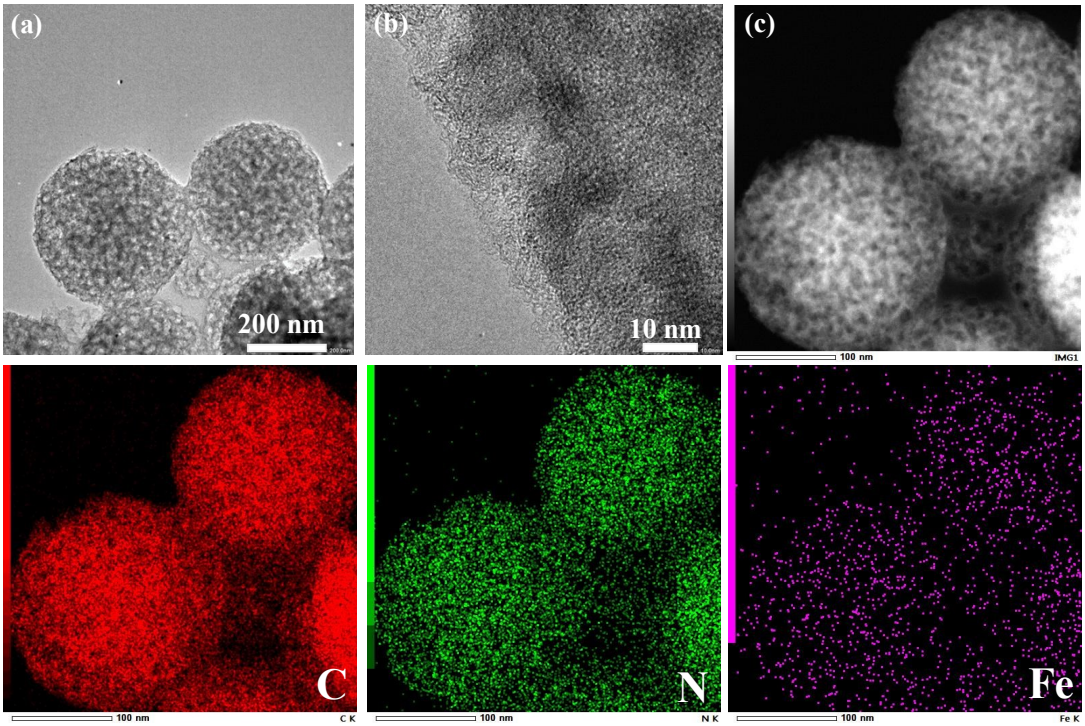

Fig. S36. (a-c) TEM images of Fe/N/C-HP and corresponding element mappings after running 40000 s in 0.1 M $HClO_4$.

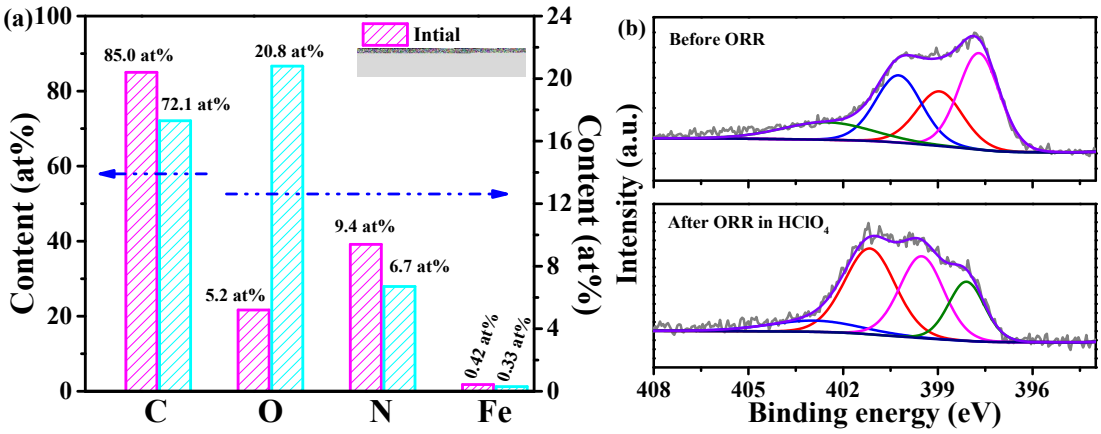

Fig. S37. (a) Elemental composition and (b) N 1s high-resolution XPS spectra of Fe/N/C-HP before and after ORR in 0.1 M $HClO_4$.

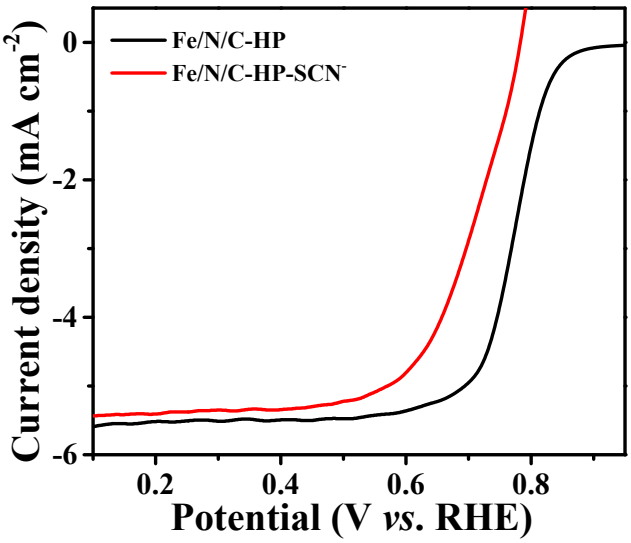

Fig. S38. Effect of SCN^- ions (10 mM) on the ORR activities of the Fe/N/C-HP in 0.1 M $HClO_4$.

Table S1. The BET surface area, total pore volume and primary mesopore diameter of catalysts.

Catalysts	$S_{BET}[m^2/g]$	$S_{micro}[m^2/g]$	$S_{meso}[m^2/g]$	$V_{total}[cm^3/g]$	$V_{micro}[cm^3/g]$	$V_{meso}[cm^3/g]$
Fe/N/C-HP	1389	665	724	1.52	0.26	1.26
Fe/N/C/NC	871	325	546	0.69	0.07	0.62

S_{BET} is the Brunauer-Emmett-Teller (BET) specific surface area.

S_{micro} is the t-plot-specific micropore surface area calculated from the N_2 adsorption-desorption Isotherm.

S_{meso} is the specific mesopore surface area estimated by subtracting S_{micro} from S_{BET}.

V_{total} is the total specific pore volume determined by using the adsorption branch of the N_2 isotherm at P/P_0=0.99 by DFT model.

V_{micro} is the specific mesopore volume obtained from the cumulative specific adsorption volume of pores of 0.00-2.00 nm in diameter.

V_{meso} is the specific micropore volume calculated by subtracting V_{micro} from V_{total}.

Table S2. The C, N, Fe and O surface content of catalysts obtained by XPS.

Sample	C	N	Fe	O	Py-N[a]	G-N[b]	Pr-N[c]	O-N
	(at%)	(at%)	(at%)	(at%)	(%)	(%)	(at%)	(at%)
Fe/N/C-HP	85.0	9.4	0.42	5.2	35.5	22.7	27.7	14.1
Fe/N/C/NC	88.2	6.0	0.89	4.9	35.2	32.1	19.7	13.0

[a] Py-N (at%) = N (at%)×Py-N (%)/100;

[a] G-N (at%) = N (at%)×G-N (%)/100;

[c] Pr-N (at%) = N (at%)×Pr-N (%)/100.

Table S3. EXAFS fitting parameters at the Fe K-edge for Fe/N/C-HP.

Sample	path	N [a]	R(Å) [b]	$\sigma^2\times10^3$(Å^2) [c]	R factor
Fe/N/C-HP	Fe-N(O)	5.1±0.3	1.98±0.01	10.3±1.3	0.0009

[a] N : coordination numbers; [b] R: bond distance; [c] σ^2: Debye-Waller factor.

Table S4. Comparison of ORR activities with the reported catalysts in alkaline media (0.1 M KOH).

Catalyst	$E_{1/2}$ vs. RHE	$\Delta E_{1/2}$ (mV) [a)]	Durability (%)	Electrolyte	References
Fe–N–C HNSs	0.87	30	91% (after 20,000 s)	0.1 M KOH	[4]
Fe–NC SAC	0.90	50	a negligible decay (after 5000 cycles)	0.1 M KOH	[5]
Fe-N/C	0.895	50	94.6% (after 30,000 s)	0.1 M KOH	[6]
C-FeZIF-1.44-950	0.864	50	96% (after 20,000 s)	0.1 M KOH	[7]
FeNx-PNC	0.86	77	93.3% (after 10,000 s)	0.1 M KOH	[8]
PNFc-900	0.86	20	86% (after 20,000 s)	0.1 M KOH	[9]
Fe−N/C	0.85	40	89% (after 20,000 s)	0.1 M KOH	[10]
Fe/N/C-HP	0.90	50	94.8% (after 40,000 s)	0.1 M KOH	This work

Table S5. Comparison of the ORR activity between Fe/N/C-HP and other catalysts in alkaline media (0.1 M KOH).

Electrocatalysts	Half-wave potential vs (RHE)	Specific activity vs RHE	Loading ($mg \cdot cm^{-2}$)	Reference
Cu SAs/N-C	0.895	5×10^{-3} mA cm^{-2}_{ECSA} at 0.9 V	0.09	[11]
FeN_x/C catalyst	0.82	1.45×10^{-4} mA cm^{-2}_{ECSA} at 0.9 V	0.6	[12]
Fe single atoms	0.92	2×10^{-3} mA cm^{-2}_{ECSA} at 0.9 V	0.3	[13]
Co SAs/N-C(900)	0.88	3×10^{-4} mA cm^{-2}_{ECSA} at 0.9 V	0.408	[14]
ZIF/ppy-pani-750	0.86	0.058 mA cm^{-2}_{ECSA} at 0.8 V	0.24	[15]
$CaMnO_{2.77}$	0.84	0.092 mA cm^{-2}_{ECSA} at 0.7 V	0.072	[16]
NCNTFs	0.87	2.1×10^{-3} mA cm^{-2}_{ECSA} at 0.9 V	0.2	[17]
pCNT@$Fe_{1.5}$@GL	0.81	4.3×10^{-4} mA cm^{-2}_{ECSA} at 0.9 V	0.2	[18]
np-MnO_2-ns	0.73	8.4×10^{-3} mA cm^{-2}_{ECSA} at 0.8 V	0.3	[19]
PtCo/Co@NHPCC	0.88	0.876 mA cm^{-2}_{Pt} at 0.9 V	6.5×10^{-3}	[20]
Fe/N/C-HP	0.90	5.7×10^{-3} mA cm^{-2}_{ECSA} at 0.9 V	0.6	This work

Table S6. Comparison of ORR activities with the reported catalysts in acid media.

Catalyst	$E_{1/2}$ vs. RHE	$\Delta E_{1/2}$ (mV) [a)]	Durability (%)	Electrolyte	References
FeSA-G	0.804	0.004	--	0.1 M $HClO_4$	[9]
C-FeZIF-1.44-950	0.78	-60	90% (after 20,000 s)	0.1 M $HClO_4$	[7]
Fe–N-CNF	0.74	-30	96% (after 10,000 s)	0.1 M $HClO_4$	[21]
Fe-N/C	0.735	-39	--	0.5 M H_2SO_4	[22]
Fe-ZIF (50 nm)	0.85	-30	20 mV decay (after 5000 cycles)	0.5 M H_2SO_4	[23]
C-FeZIF-900	0.77	-80	93% (after 20,000 s)	0.1 M $HClO_4$	[24]
Fe_2-N-C	0.78	-20	20 mV decay (after 20,000 cycles)	0.5 M H_2SO_4	[25]
Fe/N/C-HP	0.78	-50	95.4% (after 40000 s)	0.1 M $HClO_4$	This work

a) $\Delta E_{1/2} = E_{1/2\text{-sample}} - E_{1/2\text{-Pt/C}}$

Reference:

[1] J.-G. Wang, H.-J. Zhou, P.-C. Sun, D.-T. Ding, and T.-H. Chen, *Chem. Mater.,* 2010, **22**, 3829-3831

[2] C.-L. McCrory, S. Jung, J.-C. Peters and T.-F. Jaramillo, *J. Am. Chem. Soc.,* 2013, **135**, 16977.

[3] X. Fu, F.-M. Hassan, P. Zamani, G. Jiang, D.-C. Higgins, J.-Y. Choi, X. Wang, P. Xu, Y. Liu and Z. Chen, *Nano Energy,* 2017, **42**, 249-256.

[4] Y. Chen, Z. Li, Y. Zhu, D. Sun, X. Liu, L. Xu and Y. Tang, *Adv. Mater.,* 2019, **31**, 1806312.

[5] L. Zhao, Y. Zhang, L.-B. Huang, X.-Z. Liu, Q.-H. Zhang, C. He, Z.-Y. Wu, L.-J. Zhang, J. Wu, W. Yang, L. Gu, J.-S. Hu and L.-J. Wan, *Nat. Commun.,* 2019, **10**, 1278.

[6] W. Wei, X. Shi, P. Gao, S. Wang, W. Hu, X. Zhao, Y. Ni, X. Xu, Y. Xu, W. Yan, H. Ji and M. Cao, *Nano. Energy*, 2018, **52**, 29-37.

[7] Y. Deng, B. Chi, J. Li, G. Wang, L. Zheng, X. Shi, Z. Cui, L. Du, S. Liao, K. Zang, J. Luo, Y. Hu and X. Sun, *Adv. Energy Mater*., 2019, **9**, 1802856.

[8] W. Niu, L. Li, X. Liu, N. Wang, J. Liu, W. Zhou, Z. Tang and S. Chen, *J. Am. Chem. Soc*., 2015, **137**, 5555-5562.

[9] Y. Cheng, S. He, S. Lu, J.-P. Veder, B. Johannessen, L. Thomsen, M. Saunders, T. Becker, R. De Marco, Q. Li, S.-Z. Yang and S.-P. Jiang, *Adv. Sci*., 2019, **6**, 1802066.

[10] J.-C. Li, M. Cheng, T. Li, L. Ma, X. Ruan, D. Liu, H.-M. Cheng, C. Liu, D. Du, Z.-D Wei, Y.-H. Lin and M.-H. Shao, *J. Mater. Chem. A*, 2019, **7**, 14478-14482.

[11] Y. Qu, Z. Li, W. Chen, Y. Lin, T. Yuan, Z. Yang, C. Zhao, J. Wang, C. Zhao, X. Wang, F. Zhou, Z. Zhuang, Y. Wu and Y. Li, *Nat. Catal.,* 2018, **1**, 781-786.

[12] Q. Wang, Z. Zhou, Y. Lai, Y. You, J.-G. Liu, X.-L. Wu, E. Terefe, C. Chen, L. Song, M. Rauf, N. Tian and S.-G. Sun, *J. Am. Chem. Soc.,* 2014, **136**, 10882-10885.

[13] J. Wang, G. Han, L. Wang, L. Du, G. Chen, Y. Gao, Y. Ma, C. Du, X. Cheng, P. Zuo and G. Yin, *Small*, 2018, **14**, 1704282.

[14] S. Haubenreisser, T.-H. Woste, C. Martinez, K. Ishihara and K. Muniz, *Nat. Mater.,* 2011, **10**, 780.

[15] J. Tan, X. He, F. Yin, B. Chen, X. Liang, G. Li and H. Yin, *Int. J. Hydrogen Energy*, 2020, **45**, 15453-15464.

[16] J. Du, T. Zhang, F. Cheng, W. Chu, Z. Wu and J. Chen, *Inorg. Chem,* 2014, ***53***, 9106.

[17] B.-Y. Xia, Y. Yan, N. Li, H.-B. Wu, X.-W. Lou and X. Wang, *Nat. Energy*, 2016, **1**, 15006.

[18] S.-H. Ahn, X. W. Yu and A. Manthiram, *Adv. Mater*., 2017, **29**, 1606534.

[19] T. Zhang, X. Ge, Z. Zhang, N.-N. Tham, Z. Liu, A. Fisher and J.-Y. Lee, *ChemCatChem,* 2018, **10**, 422-429.

[20] J. Ying, J. Li, G. Jiang, Z.-P. Cano, Z. Ma, C. Zhong, D. Su and Z. Chen, *Appl. Catal. B: Environ.,* 2018, **225**, 496-503.

[21] B. Hu, Z. Wu, S. Chu, H. Zhu, H. Liang, J. Zhang and S. Yu, *Energy Envir. Sci*., 2018, **11**, 2208-2215.

[22] Q. Lai, L. Zheng, Y. Liang, J. He, J. Zhao and J. Chen, *ACS Catal*., 2017, **7**, 1655-1663.

[23] H. Zhang, S. Hwang, M. Wang, Z. Feng, S. Karakalos, L. Luo, Z. Qiao, X. Xie, C. Wang, D. Su, Y. Shao and G. Wu, *J. Am. Chem. Soc*., 2017, **139**, 14143-14149.

[24] Y. Deng, Y. Dong, G. Wang, K. Sun, X. Shi, L. Zheng, X. Li and S. Liao, *ACS Appl. Mater. Interfaces,* 2017, **9**, 9699-9709.

[25] W. Ye, S. Chen, Y. Lin, L. Yang, S. Chen, X. Zheng, Z. Qi, C. Wang, R. Long, M. Chen, J. Zhu, P. Gao, L. Song, J. Jiang and Y. Xiong, *Chem*, 2019, **5**, 1-14.